solids

MDPI

Article

Optimizing Organic Photovoltaic Efficiency Through Controlled Doping of ZnS/Co Nanoparticles

Jude N. Ike * and Raymond Tichaona Taziwa

Department of Applied Sciences, Faculty of Natural Sciences, Walter Sisulu University, Old King William Town Road, Potsdam Site, East London 5200, South Africa; rtaziwa@wsu.ac.za

* Correspondence: jike@wsu.ac.za

Abstract

Thin-film organic solar cells (TFOSCs) are gaining momentum as next-generation photovoltaic technologies due to their lightweight nature, mechanical flexibility, and low cost-effective fabrication. In this pioneering study, we report for the first time the incorporation of cobalt-doped zinc sulfide (ZnS/Co) nanoparticles (NPs) into a poly(3-hexylthiophene) (P3HT) and [6,6]-phenyl-C61-butyric acid methyl ester (PC61BM) bulk-heterojunction photoactive layer. ZnS/Co NPs were successfully synthesized via a wet chemical method and integrated at varying concentrations (1%wt, 3%wt, and 5%wt) to systematically investigate their influence on device performance. The optimal doping concentration of 3%wt yielded a remarkable power conversion efficiency (PCE) of 4.76%, representing a 102% enhancement over the pristine reference device (2.35%) under ambient laboratory conditions. The observed positive trend is attributed to the localized surface plasmon resonance (LSPR) effect and near-field optical enhancement induced by the presence of ZnS/Co NPs in the active layer, thereby increasing light-harvesting capability and exciton dissociation. Comprehensive morphological and optical characterizations using high-resolution scanning electron microscopy (HRSEM), high-resolution transmission electron microscopy (HRTEM), and spectroscopic techniques confirmed uniform nanoparticle dispersion, nanoscale crystallinity, and effective light absorption. These findings highlight the functional role of ZnS/Co NPs as dopants in enhancing TFOSC performance, providing valuable insights into optimizing nanoparticle concentration. This work offers a scalable and impactful strategy for advancing high-efficiency, flexible, and wearable organic photovoltaic devices.

Keywords: localized surface plasmon resonance; cobalt-doped zinc sulfide nanoparticles (ZnS/Co NPs); thin-film organic solar cells (TFOSCs); device fabrication; power conversion efficiency (PCE)

check for updates

Academic Editor: Antonio Polimeni

Received: 5 November 2025
Revised: 8 December 2025
Accepted: 9 December 2025
Published: 11 December 2025

Citation: Ike, J.N.; Taziwa, R.T. Optimizing Organic Photovoltaic Efficiency Through Controlled Doping of ZnS/Co Nanoparticles. *Solids* **2025**, *6*, 69. https://doi.org/10.3390/solids6040069

Copyright: © 2025 by the authors. Licensee MDPI, Basel, Switzerland. This article is an open access article distributed under the terms and conditions of the Creative Commons Attribution (CC BY) license (https://creativecommons.org/licenses/by/4.0/).

1. Introduction

With growing concerns over climate change and energy security, solar energy has emerged as a leading candidate among renewable energy sources due to its abundance, cleanliness, and sustainability. As global demand for environmentally friendly energy alternatives continues to rise, the development of cost-effective solar technologies that can efficiently convert sunlight into electricity becomes increasingly critical. Among various options, organic solar cells (OSCs), particularly polymer solar cells (PSCs), have gained significant attention owing to their low fabrication costs, lightweight nature, and mechanical flexibility. These features enable vacuum-free processing and compatibility with thin-film deposition techniques, making OSCs ideal for scalable, portable, and flexible

solar energy applications [1–7]. Recent advancements in material design, device architecture, and characterization have led to substantial improvements in OSC performance. Notably, power conversion efficiencies (PCEs) exceeding 20% have been achieved in devices employing non-fullerene acceptors, positioning OSCs as competitive alternatives to conventional silicon-based solar cells [8,9]. Most high-performance OSCs are based on the bulk-heterojunction (BHJ) architecture, where a conjugated donor polymer and a soluble acceptor, typically a fullerene derivative, are blended to form a nanoscale interpenetrating network that facilitates efficient exciton dissociation and charge transport [10]. Despite these achievements, OSCs still face intrinsic limitations. The photoactive layer exhibits relatively low absorption in the near-infrared (NIR) region, resulting in incomplete light harvesting [10]. Moreover, the inherently low charge carrier mobilities of organic materials restrict the thickness of the active layer. While thinner layers suffer from insufficient light absorption, thicker layers are prone to increased bulk recombination losses, both of which compromise device efficiency [11]. To address these challenges, various light-trapping strategies have been explored to enhance photon absorption within thin active layers. These include the use of optical spacer layers [12], photonic crystals [12], diffraction gratings [12], and, more recently, metallic nanoparticles (NPs) [13–18]. Metallic NPs offer a promising route to improve light harvesting through localized surface plasmon resonance (LSPR), which amplifies the local electromagnetic field and enhances light absorption. Table 1 provides an overview of representative studies that highlight the effects of incorporating metallic NPs on the performance metrics of OSCs in various device architectures.

Table 1. Provides an overview of prior studies on metallic nanoparticles (NPs) and highlights their corresponding efficiency improvements in TFOSCs.

Device Architecture	NPs	NPs Location	PCE (%) Without NPs	PCE (%) with NPs	Ref.
ITO/PEDOT:PSS/P3HT:PCBM:NPs/LiF/Al	Ag/Mg	P3HT/PCBM	2.29	4.11	[18]
ITO/PEDOT:PSS:CuS/P3HT:PC61BM:NPs/LiF/Al	CuS	PEDOT:PSS	2.01	4.51	[19]
ITO/PEDOT:PSS/P3HT:PCBMNP/LiF/Al	ZnS	P3HT:PCBM	1.90	4.00	[20]
ITO/ZnO/PTB7:PCBM/MoO_3/Al	Ag	ZnO	6.53	7.25	[21]
ITO/PEDOT:PSS/PTB7:PC71BM/Ca/Al	Au@Ag@SiO_2	PTB7:PC71BM	7.72	9.56	[22]
ITO/ZnS/Y_2O_3/PTB7:PC71BM/MoO_3/Ag	ZnO/Y_2O_3	ZnO	5.77	6.22	[23]
ITO/PEDOT:PSS:Au/PTB7:PC71BM/Ca	Au	PEDOT:PSS	7.50	8.10	[24]
ITO/PEDOT:PSS/PTB7:PC71BM/Ca/Al	Au@Ag@SiO_2	PEDOT:PSS	7.72	9.04	[22]

Additionally, their scattering properties extend the optical path length, increasing exciton generation and improving charge transport. Beyond noble metals, various metal and semiconductor sulfide NPs, including copper sulfide (CuS) [25], zinc oxide (ZnO) [26], and zinc sulfide (ZnS) [20], have shown promise in enhancing OSC performance. More recently, cobalt (Co) doping has emerged as a strategy to further improve the optoelectronic properties of metal NPs, thereby increasing their effectiveness in photovoltaic applications [27]. To the best of our knowledge, this study is the first to report the incorporation of cobalt-doped zinc sulfide (ZnS/Co) NPs into a P3HT/PC61BM polymer blend as the active layer in OSCs. The introduction of ZnS/Co NPs significantly enhanced the optical absorption of the photoactive film, leading to improved exciton generation and charge transport. These enhancements led to a notable improvement in overall device performance, as discussed in the following sections.

2. Materials and Methods Section

2.1. Materials

All chemical reagents used for the synthesis of cobalt-doped zinc sulfide (ZnS/Co) NPs were obtained from commercial suppliers and used without further purification. The precursors included sodium borohydride ($NaBH_4$, >99.98%), cobalt nitrate ($Co(NO_3)_2$, >98%), zinc nitrate ($Zn(NO_3)_2$, >99.98%), and thiourea (CH_4N_2S), all purchased from Sigma-Aldrich (St. Louis, MO, USA). Polymer materials employed in device fabrication, including poly-(3,4-ethylene dioxythiophene): poly-(styrene-sulfonate) (PEDOT: PSS), Poly-(3-hexylthiophene) (P3HT), and [6,6]-phenyl-C61-butyric acid methyl ester (PC61BM), each with a purity of 95%, were sourced from Ossila Co. Ltd., Sheffield (UK). Indium tin oxide (ITO)-coated glass substrates, with a sheet resistance of 8–12 Ω/sq, were also procured from Ossila.

2.2. Synthesis of ZnS/Co NPs

The ZnS/Co NPs were synthesized using a wet chemical processing method, which was selected for its simplicity and ability to achieve controlled doping, a critical step in tuning the optical and electronic properties of the resulting NPs. In this procedure, aqueous solutions of zinc nitrate (40 mM), thiourea (40 mM), cobalt nitrate (20 mM), and sodium borohydride (0.5 M) were prepared by dissolving each compound in 50 mL of deionized (DI) water in separate clean flasks. The synthesis began by sequentially adding the zinc nitrate and thiourea solutions into a 500 mL beaker under continuous stirring. Following this, the cobalt nitrate solution was introduced dropwise to ensure uniform distribution of the dopant within the reaction medium. Subsequently, sodium borohydride was added as a reducing agent to initiate the formation of nanoparticles. The reaction mixture was stirred continuously on a magnetic hot plate for 4 h at an average temperature of 45 °C to promote homogeneity and facilitate the formation of ZnS/Co NPs. After synthesis, the resulting suspension was repeatedly washed and filtered with DI water to remove residual sodium ions and other byproducts. The purified product was then dried in a vacuum oven at 80 °C for 2 h, yielding ZnS/Co NPs suitable for incorporation into the active layer of OSCs.

2.3. Device Fabrication of ZnS/Co NPs

The patterned ITO-coated glass was first etched using an acid solution composed of HCl, H_2O, and HNO_3 in a volume ratio of 48:48:4. Following etching, the substrates were thoroughly cleaned by sequential sonication in DI water, acetone, and isopropanol for 15 min each, followed by drying at 100 °C in an oven. The conventional device architecture employed in this study was Glass/ITO/PEDOT:PSS/P3HT:PC61BM+ZnS/Co/LiF/Al, as illustrated in Figure 1.

A thin hole-extraction layer of PEDOT: PSS was deposited onto the ITO-coated glass by spin-coating at 3500 rpm for 1 min, followed by drying in an oven at 90 °C for 25 min under ambient conditions. The P3HT and PC61BM blended solution, with a concentration of 20 mg/mL, was prepared by dissolving the active layer in a mixed solvent of chloroform at a ratio of 1:1 by weight. However, ZnS/Co NPs were incorporated into the mixture solution at concentrations of 1%wt, 3%wt, and 5%wt, with each concentration prepared in a separate solution. The mixtures were stirred on a hot plate at 45 °C for 4 h to ensure homogeneity. The photoactive layer with incorporated ZnS/Co NPs at different concentrations were mainly spin-coated onto the PEDOT: PSS layer at 1200 rpm for 40 s and subsequently dried in a furnace at 90 °C for 6 min under a nitrogen atmosphere. Finally, a thin layer of lithium fluoride (LiF, 0.5 nm) and an aluminum (Al) electrode (70 nm) were deposited in a vacuum chamber at a pressure of 10^{-6} mbar.

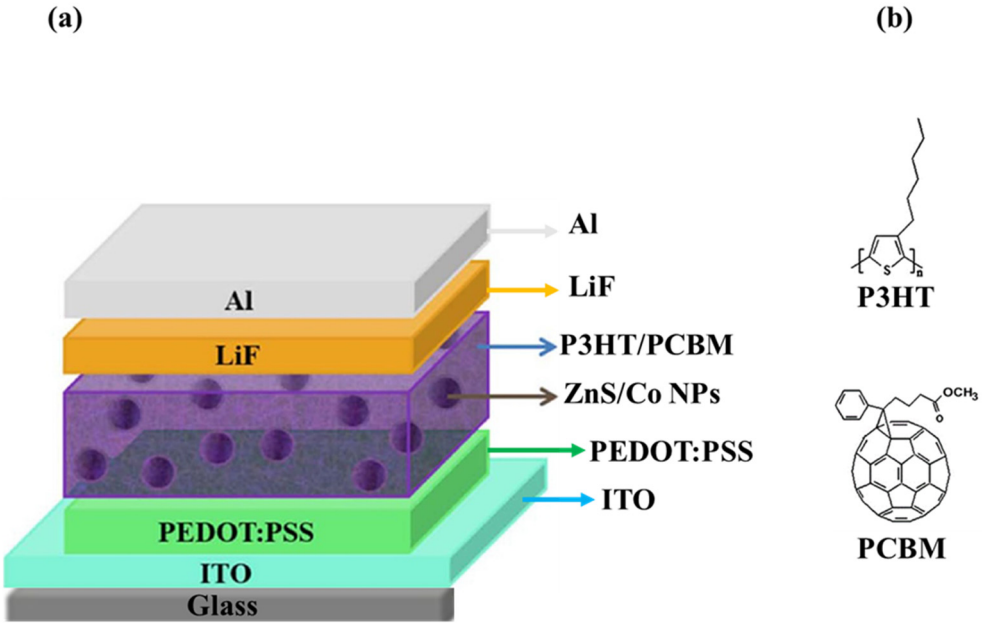

Figure 1. (**a**) Schematic diagram of the thin-film organic solar cell (TFOSC) device architecture incorporating cobalt-doped ZnS nanoparticles (ZnS/ Co NPs). (**b**) Chemical structures of the donor polymer P3HT and acceptor molecule PCBM used in the photoactive layer.

2.4. Device Characterization Section

The current density–voltage (*J–V*) characteristics of the fabricated organic solar cells were measured using a Keithley HP2420 source meter in conjunction with a solar simulator (model SS50AAA) operating under standard AM1.5G illumination at an intensity of 100 mW/cm^2. These measurements were conducted to evaluate the photovoltaic performance of the devices. Space-charge-limited current (SCLC) is measured under dark conditions using a solar simulator to investigate the effect of photon-generated traps in polymer solar cells. The optical properties of the photoactive films, including absorption behavior, were characterized using ultraviolet–visible (UV–Vis) spectroscopy. This analysis provided insights into the light-harvesting capabilities of the active layers and the influence of ZnS/Co NPs incorporation on the spectral response. High-resolution scanning electron microscopy (HRSEM) and high-resolution transmission electron microscopy (HRTEM) utilize advanced imaging strategies, signal-detection modes, and complementary analytical techniques to investigate materials or samples at the nanoscale, often achieving atomic-level resolution. Energy-dispersive X-ray spectroscopy (EDX) was employed to determine the percentage composition of the nanoparticles. Fourier transform infrared spectrophotometer (FTIR) is a notable technique used to determine additional aspects of the prepared nanostructures by identifying their characteristic peaks and confirming the sample's functional groups and chemical structure.

3. Results and Discussion Section

3.1. Morphological and Structural Characterization of Cobalt-Doped ZnS NPs

To gain comprehensive insights into the morphology and internal structure of the synthesized ZnS/Co NPs, both high-resolution scanning electron microscopy (HRSEM) and high-resolution transmission electron microscopy (HRTEM) analyses were conducted. HRSEM imaging revealed a relatively uniform distribution of nanoparticles, exhibiting a mixture of disc-like and spherical morphologies. This uniformity suggests a well-controlled synthesis process and is essential for ensuring homogeneous dispersion within the polymer matrix, minimizing aggregation-related losses, and promoting consistent device perfor-

mance. Similar morphologies have been reported in ZnS nanocrystals synthesized via wet chemical methods, indicating that the observed shapes are typical of this synthesis route [20]. HRTEM analysis provided detailed structural information, revealing well-defined lattice fringes with interplanar spacings of 0.310 nm and 0.266 nm, as clearly observed in Figure 2a. These values correspond to the (111) and (200) planes of cubic ZnS, respectively, and are consistent with those reported in previous studies on ZnS and Co-doped ZnS nanocrystals [20,28,29]. Notably, the HRTEM images also revealed features indicative of core–shell-like structures, characterized by a darker central region surrounded by lighter shells, as shown in Figure 2a–c, with relative distribution in terms of size and shape.

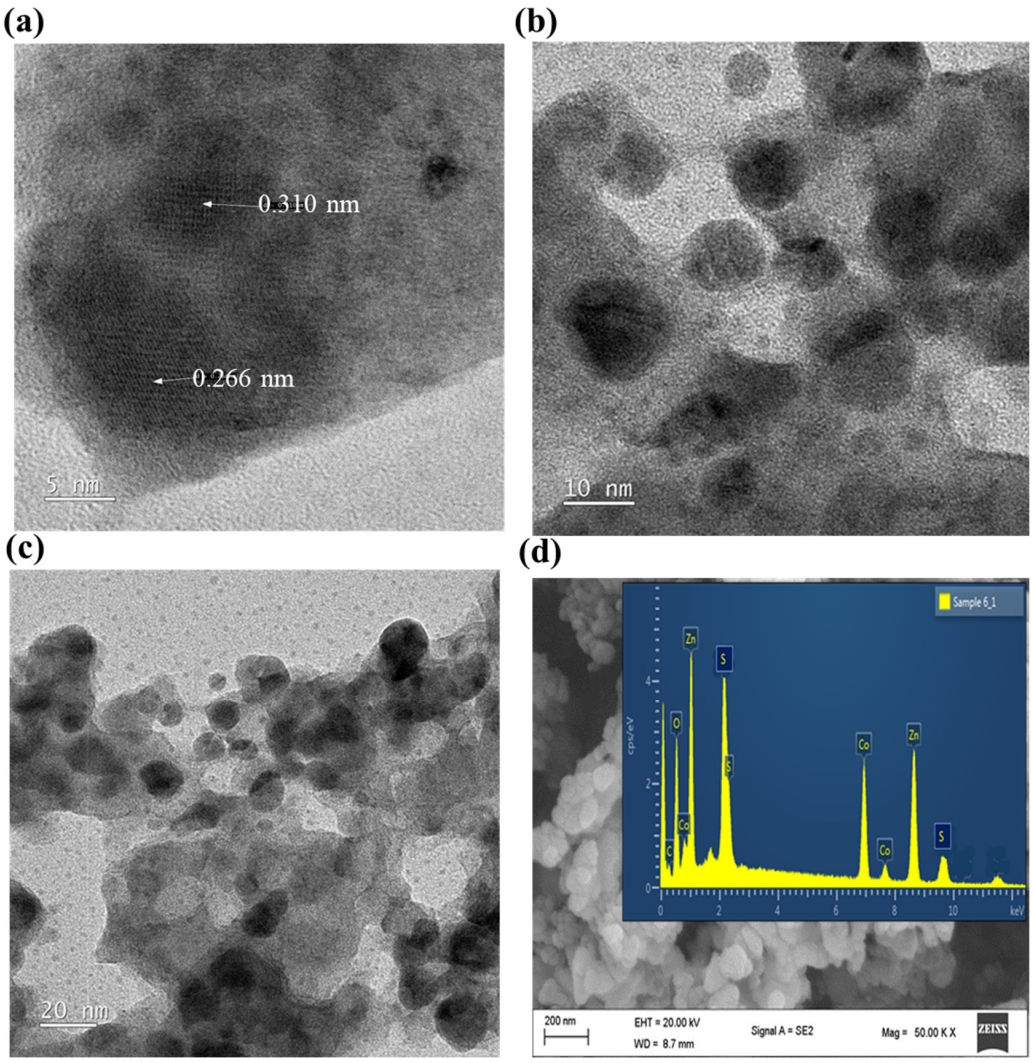

Figure 2. (**a**–**c**) Demonstrate the HRTEM images of the synthesized ZnS/Co NPs. (**d**) High-resolution scanning electron microscopy (HRSEM) image with an inset displaying the energy-dispersive X-ray (EDX) spectrum, confirming elemental composition.

This morphology may result from compositional gradients or differences in atomic density between the ZnS core and the Co-doped shell. The particle size distribution, estimated from HRTEM images, ranged between 5 and 10 nm. This nanoscale dimension is particularly advantageous for organic solar cell applications, as it facilitates intimate contact with the polymer matrix, enhances interfacial charge transfer, and supports efficient exciton dissociation. Nanoparticles within this size range have been shown to integrate well into polymer blends, maintaining phase stability and promoting effective charge

transport [20]. Elemental analysis using HRSEM coupled with energy-dispersive X-ray spectroscopy (EDX), shown in the inset of Figure 2d, confirmed the presence and uniform distribution of zinc (Zn), sulfur (S), and cobalt (Co) throughout the sample. The distinct intensity peaks corresponding to these elements provide strong evidence for the successful formation of ZnS/Co NPs. The detection of cobalt alongside Zn and S supports the effective incorporation of the dopant into the ZnS matrix, which is essential for tailoring the optical and electronic properties of the nanoparticles. A minor carbon (C) signal was also observed, likely due to partial surface oxidation or ambient contamination during sample handling, a common occurrence in nanoparticle characterization. The elemental uniformity observed in the EDX mapping further reinforces the structural homogeneity of the synthesized ZnS/Co NPs, which are critical for consistent performance when integrated into the active layer of OSC devices.

3.2. Fourier Transform Infrared Spectrophotometer of ZnS/Co NPs

The chemical structures of the synthesized ZnS/Co NPs were investigated using a Fourier transform infrared spectrophotometer (FTIR), with the results presented in Figure 3. The successful synthesis of ZnS/Co NPs were confirmed through FTIR spectroscopy, which provided critical insights into both the structural framework and surface chemistry of the material. The vibrational signatures observed in the FTIR spectrum serve as compelling evidence for the formation of the ZnS lattice and the effective incorporation of cobalt dopants.

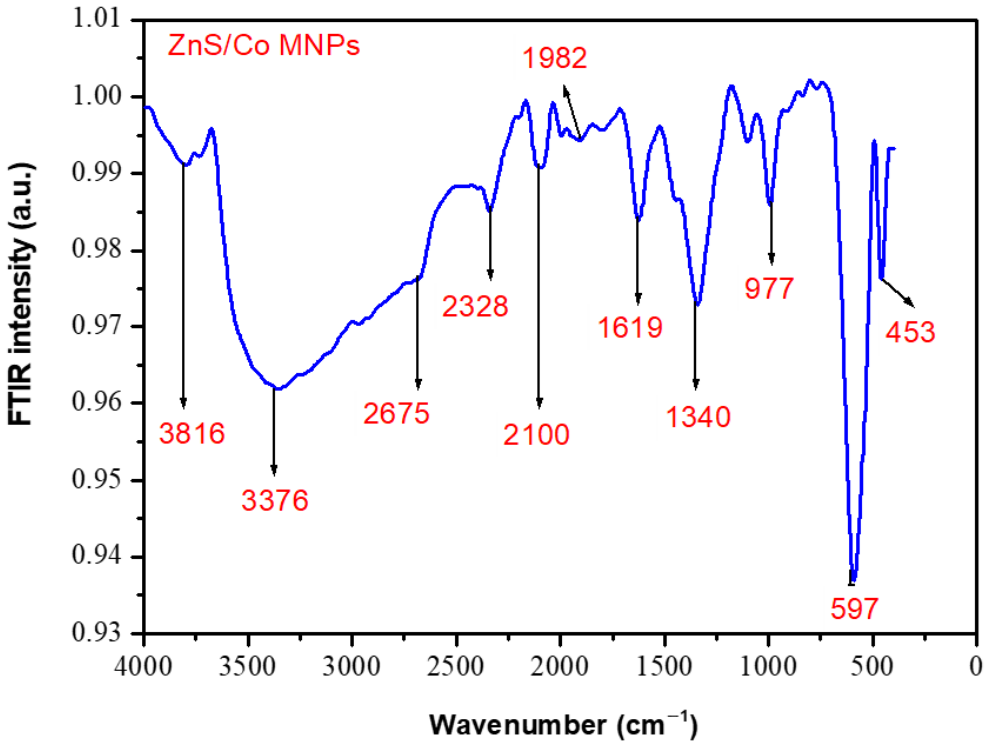

Figure 3. Shows the Fourier transform infrared (FTIR) spectrum of ZnS/Co NPs, indicating the characteristic of Zn–S stretching vibrations and surface-bound functional groups indicative of successful synthesis and cobalt incorporation.

In the low-wavenumber region, the spectrum displayed distinct absorption peaks at 597 cm^{-1} and 453 cm^{-1}, which are characteristic of Zn–S stretching vibrations. These peaks fall within the well-established range of 400–706 cm^{-1}, commonly associated with Zn–S bond formation. Notably, the peak at 597 cm^{-1} aligns with previously reported values for Co-doped ZnS systems, typically observed between 500 and 650 cm^{-1} [30–33]. Such vibrational modes have been documented in the literature [33], including peaks

at 662 cm^{-1} and 467 cm^{-1}, further reinforcing the conclusion that the ZnS lattice was successfully formed and structurally stabilized by the incorporation of Co. Complementing the FTIR findings, HRTEM analysis provided detailed structural insights, revealing well-defined lattice fringes with interplanar spacings of 0.310 nm and 0.266 nm. These spacings correspond to the (111) and (200) planes of cubic ZnS, respectively. The consistency between the vibrational signatures observed in FTIR and the crystallographic features revealed by HRTEM confirms the successful synthesis and structural integrity of the Co-doped ZnS lattice. Beyond structural confirmation, the mid- to high-frequency regions of the FTIR spectrum provided valuable information regarding surface-bound functional groups and residual species. A broad absorption band at 3376 cm^{-1} was attributed to O–H stretching vibrations, indicative of surface-adsorbed water molecules or hydroxyl groups. These functional groups are known to play a pivotal role in photocatalytic processes, particularly in the generation of reactive hydroxyl radicals (•OH) under irradiation. The peak at 1619 cm^{-1} was assigned to H–O–H bending vibrations of molecular water or possibly C=O stretching, likely resulting from atmospheric CO_2 absorption. This peak, along with those at 977 cm^{-1} and 597 cm^{-1}, may also reflect Co(H–O–H) bending interactions, suggesting a degree of coordination between cobalt ions and water molecules on the nanoparticle surface. Additional absorption bands observed at 3816 cm^{-1}, 2675 cm^{-1}, 2328 cm^{-1}, 2100 cm^{-1}, 1982 cm^{-1}, 1340 cm^{-1}, and 977 cm^{-1} are consistent with the presence of residual water and carbon dioxide molecules, commonly introduced during synthesis or through environmental exposure. Notably, bands in the 2849–2930 cm^{-1} range correspond to C–H stretching vibrations, which may be attributed to organic residues from precursor materials or stabilizing agents used during the co-precipitation process.

3.3. Optical Absorption of the Photoactive Films

A comprehensive investigation of ZnS/Co NPs and their composite films were conducted using UV–Vis spectroscopy, a pivotal technique for elucidating the optical and electronic properties of metallic materials. Figure 4 presents the extensive absorber films, both with and without the incorporation of ZnS/Co NPs. Figure 4a shows the optical absorbance spectrum of ZnS/Co NPs powder suspended in DI water. A broad absorption peak centered around 410 nm is observed, along with continuous absorbance across the entire measured spectrum. This broad and extended absorption is attributed to the size distribution of the ZnS/Co NPs, which enhances photon absorption within the medium. Interestingly, Tauc's plot is one of the most widely used methods to estimate the optical bandgap energy, as demonstrated below:

$$\alpha h\upsilon = \beta\left(h\upsilon - E_g\right)^n \quad (1)$$

here, h is Planck's constant, υ is the photon frequency, α is the absorption coefficient, β is the material-dependent constant, E_g is the optical energy bandgap, and n is an exponent, which depends on the nature of the transition [30]. The optical E_g was investigated from the intercept of the tangent to the $(\alpha h\upsilon)$ versus $h\upsilon$ plot, extrapolated to $(\alpha h\upsilon)^2 = 0$. From this analysis, the direct bandgap of ZnS/Co NPs were observed to be 1.94 eV (see Figure 4b).

In composite films consisting of a P3HT/PCBM blend with varying concentrations of ZnS/Co NPs loading from (pristine, 1%wt, 3%wt, and 5%wt), the UV−Vis absorption spectra are predominantly influenced by the characteristic absorbance of the polymer blend, with a typical absorption peak ranging from 504 to 510 nm (see Figure 4c). However, the incorporation of ZnS/Co NPs resulted in notable spectral changes, including the emergence of additional absorption bands in the UV region, with maximum absorption occurring between 390 and 401 nm. There were also increased peak intensities and broadening of the absorption envelope across the visible and near-infrared (NIR) regions. These alter-

ations suggest enhanced light-harvesting capabilities and possible changes in the electronic structure of the composite films resulting from the presence of the metal nanoparticles. The optical absorption intensity varied with the concentration of ZnS/Co NPs in the active layer. A maximum absorption peak was observed at a concentration of 3 wt%. However, increasing the concentration to 5%wt led to a noticeable decrease in absorption intensity. This reduction is attributed to the formation of a higher density of defects within the active layer, which facilitates charge carrier recombination and subsequently reduces the optical absorption. However, Figure 4d and Table 2 reveal slight variations in the energy bandgap of the absorber films. The differences in bandgap values are due to reduced charge recombination, caused by the interaction between ZnS/Co NPs and the polymer cells. Moreover, the effective suppression of charge recombination was observed at ZnS/Co NPs doping levels of 1%wt, 3%wt, and 5%wt by weight. Consequently, photon energy loss was evaluated by analyzing the variation in the energy bandgap of the absorber films. Mathematically, it is expressed as $E_{loss} = E_g - qV_{oc}$, where qV_{oc} is the energy extracted from the cell. An increase in E_{loss} from 0.94 eV to 1.08 eV was observed across the tested solar cells, indicating a dependence on the ZnS/Co NPs' doping concentrations. However, the highest energy loss was recorded in the undoped reference device, confirming that ZnS/Co NPs help reduce energy loss by limiting charge recombination. Finally, the presence of ZnS/Co NPs promotes exciton dissociation and charge transport, thereby accounting for the observed improvement in device performance.

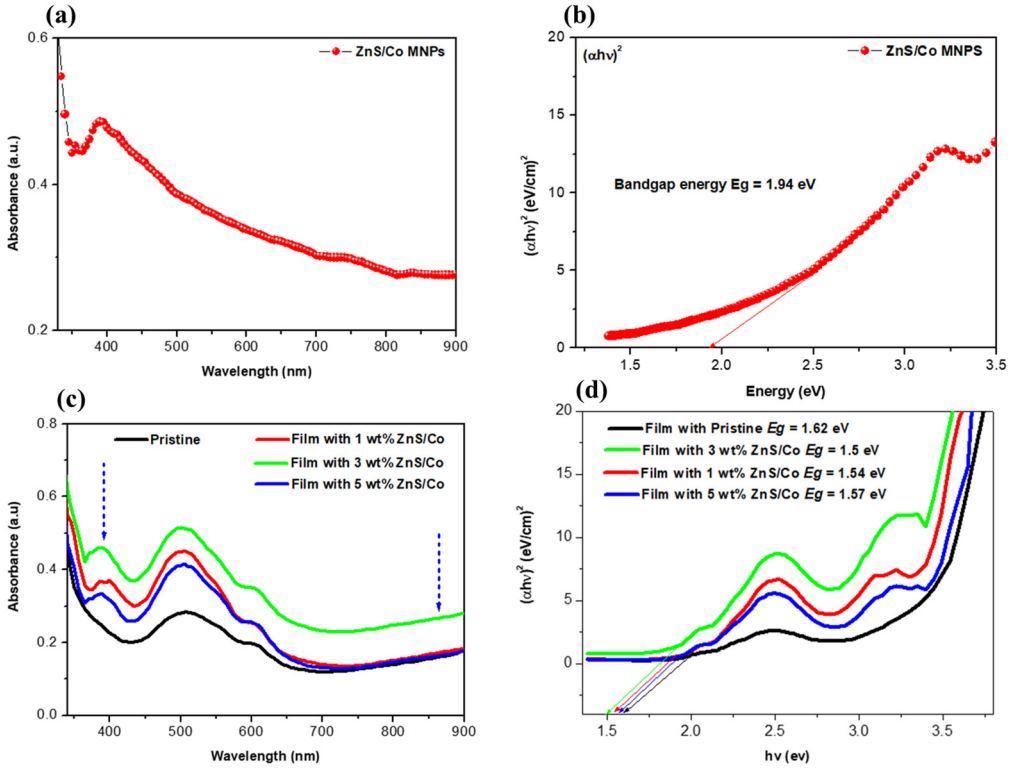

Figure 4. (**a**) Shows the optical absorption spectrum of ZnS/Co NPs in powder form, which are dispersed in deionized water. (**b**) Tauc's plot derived from the absorbance data in (**a**), used to estimate the optical bandgap of the powder suspension. (**c**) UV−Vis absorption spectra of the pristine and doped photoactive films. (**d**) Tauc's plots corresponding to the films in (**c**), used to evaluate the optical bandgap variation with doping concentration.

Table 2. The J-V performance of TFOSCs with different concentrations of ZnS/Co NPs in the P3HT/PCBM active layer.

ZnS/Co (%wt)	E_g (eV)	E_{loss} (eV)	V_{oc} (V)	J_{sc} (mAcm^{-2})	FF (%)	PCE (%)	R_s (Ωcm^2)
0%wt	1.62	1.08	0.54	10.23	44.40	2.35	850
1%wt	1.54	0.98	0.56	14.85	49.78	3.91	443
3%wt	1.50	0.94	0.56	15.71	57.41	4.76	359
5%wt	1.57	1.01	0.56	13.36	47.52	3.55	571

3.4. Electrical Properties of the Photoactive Films

It is worth noting that organic solar cells (OSCs) were fabricated with a photoactive layer composed of P3HT/PCBM as the reference device, and P3HT/PCBM doped with ZnS/Co NPs at various concentrations. The $J-V$ (current density–voltage) characteristics recorded for the newly fabricated solar cells are provided in Figure 5. The reference device, fabricated without the inclusion of ZnS/Co NPs, produced an efficiency of 2.35%, with a J_{sc} (short-circuit current density) of 10.23 mAcm^{-2}. However, a significant enhancement in device performance was observed at the doping levels of 1%wt, 3%wt, and 5%wt concentrations of ZnS/Co NPs in the photoactive layer (see Table 2). The maximum PCE value recorded in this experimental work was 4.76% at an optimal doping concentration of 3%wt. The observed enhancement is attributed to a notable increase in J_{sc} to 15.71 mAcm^{-2}, thereby providing a 53.57% improvement over the reference solar cell.

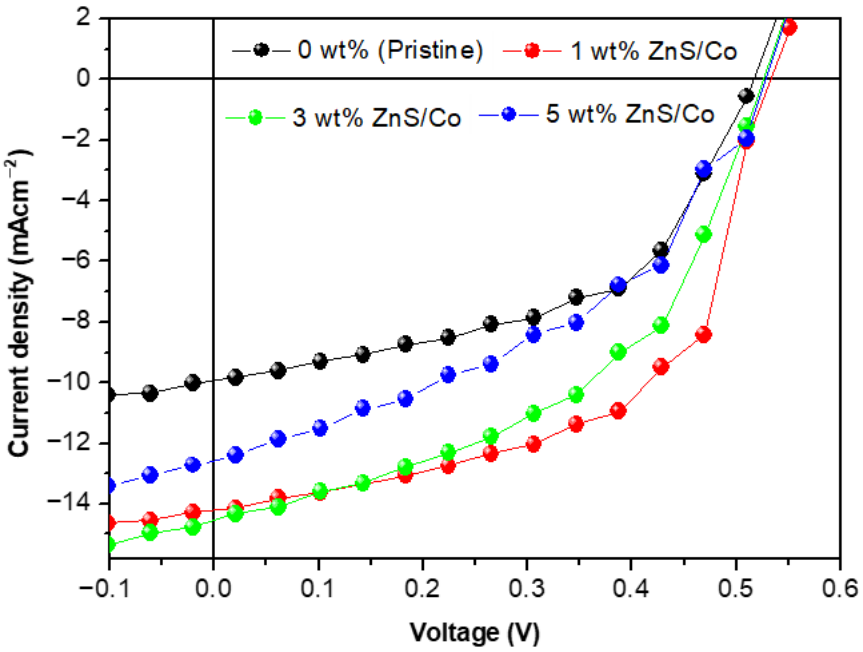

Figure 5. $J-V$ (current density–voltage) characteristics curve of OSCs fabricated with and without ZnS/Co NPs measured under standard AM1.5G illumination, showing performance improvements across different doping levels.

The increase in device performance is generally credited to the improved photocurrent collection, facilitated by the incorporation of ZnS/Co NPs. The observed positive trend is attributed to the LSPR effect and near-field optical enhancement induced by the presence of ZnS/Co NPs in the active layer, thereby increasing light-harvesting capability. This is supported by UV-Vis spectral data, which show the highest intensity peak absorption at a 3%wt NP loading (see Figure 4c), promoting exciton dissociation and enhancing charge carrier collection. As shown in Table 2, the fill factor (FF) increased from 44.40%

in the reference device to 57.41% at a 3%wt doping, indicating reduced internal power losses. This improvement in FF is correlated with a significant reduction in current leakage, facilitated by near-field effects that promote more efficient exciton dissociation [34,35], as well as a lower series resistance (R_s), which decreased from 850 Ωcm^2 to 359 Ωcm^2. Additionally, the photon energy loss (E_{loss}) decreased from 1.08 eV in the pristine device to 0.94 eV at optimal doping, suggesting more efficient charge separation and suppressed recombination (see Table 2). Finally, the high conductivity and electron mobility of ZnS/Co NPs are instrumental in this reduction, as they integrate seamlessly into the polymer matrix, facilitating charge extraction. These findings clearly demonstrate that incorporating ZnS/Co NPs into the P3HT/PC61BM photoactive layer enhances its optical absorption and establishes favorable conditions for exciton dissociation and charge transport, resulting in improved photon harvesting in polymer solar cells.

3.5. Charge Transport Properties of the Photoactive Films

Understanding the electrical properties of polymer solar cells critically depends on analyzing charge transport processes. In thin-film organic solar cells (TFOSCs), the space-charge-limited current (SCLC) regime provides a reliable method for evaluating charge transport characteristics within the photoactive layer. To reduce the effect of photon-generated traps, the SCLC measurements were conducted under dark conditions (see Figure 6a). This approach ensures that the extracted charge transport parameters more appropriately reflect the intrinsic properties of the samples. Figure 6b shows the SCLC characteristics derived from the forward bias region of the dark $J-V$ curve, beginning at the injection-limited regime around 1.54 V and extending to the point where current saturation occurs.

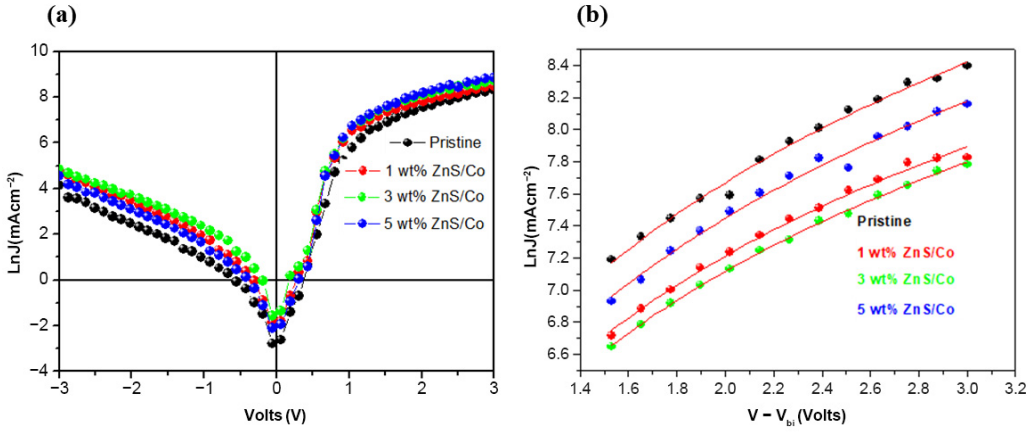

Figure 6. (**a**) $J-V$ characteristics under dark conditions, and (**b**) SCLC fitted with Mott–Gurney's law for the reference device and various concentrations of ZnS/Co NPs in the active layer.

The SCLC data were subsequently fitted using the field-dependent mobility model, as described by Mott–Gurney's law (Equation (1)) [36,37].

$$J_{SCLC} = \frac{9}{8}\varepsilon\varepsilon_0\mu_0\frac{V^2}{L^3}exp\left(0.89\gamma\sqrt{\frac{V}{L}}\right) \quad (2)$$

here, V is the applied voltage corrected for built-in voltage (V_{bi}), while L refers to the photoactive layer's thickness, which is 100 nm in the device. ε is the dielectric constant of the photoactive layer, and $\varepsilon_0 = 8.85 \times 10^{-12}$ F/cm, which is the permittivity of free space, while μ_0 and γ are the zero-field mobility and the field activation factor, respectively. It is worth noting that the mobility of polymer solar cells decreases at high applied electric

fields due to the negative values observed in the field activation factor, as reported in the literature [38]. The results are presented in Table 3. The results in Table 3 further indicate that the zero-field mobility is in one order of magnitude higher than that of the pristine reference solar cell, which is a clear indication that the ZnS/Co NPs embedded with an active layer at various concentrations play a significant role in enhancing charge transport and charge dissociation, due to the presence of the LSPR effect in polymer solar cells. These findings validate the efficacy of incorporating ZnS/Co nanoparticles into the active layer as a transformative strategy for enhancing the performance of organic solar cells.

Table 3. The charge transport parameters of TFOSCs fabricated at various concentration levels of ZnS/Co NPs.

ZnS/Co (%wt)	μ_0 ($cm^2S^{-1}V^{-1}$)	γ (cmV^{-1})
0%wt (Pristine)	2.6785×10^{-4}	-1.9081×10^{-4}
1%wt	1.8124×10^{-3}	-1.3114×10^{-4}
3%wt	1.7933×10^{-3}	-1.1340×10^{-4}
5%wt	1.9961×10^{-3}	-1.4072×10^{-4}

4. Conclusions

In summary, we investigated the photovoltaic performance of organic solar cells (OSCs) by incorporating ZnS/Co NPs into the P3HT/PCBM active layer. The doped photoactive layer exhibited enhanced light absorption compared to the pristine reference cell, leading to improvements in J_{sc} (short-circuit current density), (FF) fill factor, and overall power conversion efficiency (PCE). As a result, the highest PCE of 4.76% was achieved at a 3%wt concentration of ZnS/Co NPs, compared to the pristine (0%wt) device. This improvement is attributed to the LSPR effect introduced by the nanoparticles, which augments exciton dissociation and charge transport, while also reducing series resistance and increasing the device's electrical conductivity. We believe this approach offers a promising pathway for augmenting the efficiency of OSC devices and could inspire future research on solar cells utilizing non-fullerene acceptors.

Author Contributions: J.N.I.—Conceptualization; investigation; Software; Formal analysis; Data Curation; validation; visualization; writing—original draft; writing—review and editing. R.T.T.—Conceptualization; investigation; validation; funding acquisition; supervision; writing—review and editing. All authors have read and agreed to the published version of the manuscript.

Funding: This manuscript is financially supported by the National Research Foundation (NRF), South Africa (Grant numbers: 138079) and Tertiary Education Support Program (TESP), Eskom Holding SOC Limited Reg No: 2002/015527/0.

Data Availability Statement: Data presented in this work are available upon request from the corresponding author to maintain data privacy.

Conflicts of Interest: The authors declare no conflicts of interest.

References

1. Wadsworth, A.; Moser, M.; Marks, A.; Little, M.S.; Gasparini, N.; Brabec, C.J.; Baran, D.; McCulloch, I. Critical review of the molecular design progress in non-fullerene electron acceptors towards commercially viable organic solar cells. *Chem. Soc. Rev.* **2019**, *48*, 1596–1625. [CrossRef]
2. Ike, J.N.; Mola, G.T.; Taziwa, R.T. Review on Indacenodithiophene (IDT) and Perylene Diimides (PDIs) Based Non-Fullerene Acceptors in Organic Solar Cells: Progress and Challenges. *Chem. Afr.* **2025**, *8*, 2687–2705. [CrossRef]
3. Cui, Y.; Yao, H.; Zhang, J.; Xian, K.; Zhang, T.; Hong, L.; Wang, Y.; Xu, Y.; Ma, K.; An, C.; et al. Single-junction organic photovoltaic cells with approaching 18% efficiency. *Adv. Mater.* **2020**, *32*, 1908205. [CrossRef]

4. Hu, Z.; Wang, J.; Ma, X.; Gao, J.; Xu, C.; Yang, K.; Wang, Z.; Zhang, J.; Zhang, F. A critical review on semitransparent organic solar cells. *Nano Energy* **2020**, *78*, 105376. [CrossRef]
5. Wang, H.; He, Z.; Liu, X.; Xin, J.; Geng, Z.; Yang, K.; Zhang, Y.; Zhang, Y.; Duan, M.; Qin, B.; et al. Temporally stepwise crystallization via dual-additive orchestration: Resolving the crystallinity-domain size paradox for high-efficiency organic photovoltaics. *J. Energy Chem.* **2025**, *112*, 370–383. [CrossRef]
6. Yang, C.; Zhang, S.; Ren, J.; Gao, M.; Bi, P.; Ye, L.; Hou, J. Molecular design of a non-fullerene acceptor enables a P3HT-based organic solar cell with 9.46% efficiency. *Energy Environ. Sci.* **2020**, *13*, 2864–2869. [CrossRef]
7. Xu, X.; Feng, K.; Lee, Y.W.; Woo, H.Y.; Zhang, G.; Peng, Q. Subtle polymer donor and molecular acceptor design enable efficient polymer solar cells with a very small energy loss. *Adv. Funct. Mater.* **2020**, *30*, 907570. [CrossRef]
8. Sun, Y.; Wang, L.; Guo, C.; Xiao, J.; Liu, C.; Chen, C.; Xia, W.; Gan, Z.; Cheng, J.; Zhou, J.; et al. π-extended nonfullerene acceptor for compressed molecular packing in organic solar cells to achieve over 20% efficiency. *J. Am. Chem. Soc.* **2024**, *146*, 12011–12019. [CrossRef] [PubMed]
9. Jiang, Y.; Sun, S.; Xu, R.; Liu, F.; Miao, X.; Ran, G.; Liu, K.; Yi, Y.; Zhang, W.; Zhu, X. Non-fullerene acceptor with asymmetric structure and phenyl-substituted alkyl side chain for 20.2% efficiency organic solar cells. *Nat. Energy* **2024**, *9*, 975–986. [CrossRef]
10. Cheng, P.; Zhan, X. Versatile third components for efficient and stable organic solar cells. *Mater. Horiz.* **2015**, *2*, 462–485. [CrossRef]
11. Ike, J.N.; Nqoro, X.; Mola, G.T.; Taziwa, R.T. Controlling the Concentration of Copper Sulfide Doped with Silver Metal Nanoparticles as a Mechanism to Improve Photon Harvesting in Polymer Solar Cells. *Processes* **2025**, *13*, 2922. [CrossRef]
12. Ahmed, A.Y.; Ogundele, A.K.; Hamed, M.S.; Tegegne, N.A.; Kumar, A.; Sharma, G.; Mola, G.T. Application of cobalt-sulphide to suppress charge recombinations in polymer solar cell. *Mater. Sci. Semicond. Process.* **2025**, *185*, 108917. [CrossRef]
13. Notarianni, M.; Vernon, K.; Chou, A.; Aljada, M.; Liu, J.; Motta, N. Plasmonic effect of gold nanoparticles in organic solar cells. *Sol. Energy* **2014**, *106*, 23–37. [CrossRef]
14. Oseni, S.O.; Mola, G.T. Bimetallic nanocomposites and the performance of inverted organic solar cell. *Compos. Part B Eng.* **2019**, *172*, 660–665. [CrossRef]
15. Ueno, K.; Oshikiri, T.; Sun, Q.; Shi, X.; Misawa, H. Solid-state plasmonic solar cells. *Chem. Rev.* **2017**, *118*, 2955–2993. [CrossRef]
16. Mulat, S.A.; Hone, F.G.; Bekri, N.; Tegegne, N.A. Improving the light harvest of plasmonic based organic solar cells by utilizing dielectric core–Shells. *Plasmonics* **2025**, *20*, 4007–4019. [CrossRef]
17. Coviello, V.; Forrer, D.; Amendola, V. Recent developments in plasmonic alloy nanoparticles: Synthesis, modelling, properties and applications. *ChemPhysChem* **2022**, *23*, e202200136. [CrossRef]
18. Ahmed, A.Y.; Ike, J.N.; Hamed, M.S.; Mola, G.T. Silver decorated magnesium doped photoactive layer for improved collection of photo-generated current in polymer solar cell. *J. Appl. Polym. Sci.* **2023**, *140*, e53697. [CrossRef]
19. Adedeji, M.A.; Hamed, M.S.; Mola, G.T. Light trapping using copper decorated nano-composite in the hole transport layer of organic solar cell. *Sol. Energy* **2020**, *203*, 83–90. [CrossRef]
20. Dlamini, M.W.; Hamed, M.S.; Mbuyise, X.G.; Mola, G.T. Improved energy harvesting using well-aligned ZnS nanoparticles in bulk-heterojunction organic solar cell. *J. Mater. Sci. Mater. Electron.* **2020**, *31*, 9415–9422. [CrossRef]
21. Nair, A.T.; Anoop, C.S.; Vinod, G.A.; Reddy, V.S. Efficiency enhancement in polymer solar cells using combined plasmonic effects of multi-positional silver nanostructures. *Org. Electron.* **2020**, *86*, 105872. [CrossRef]
22. Liu, S.; Jiang, R.; You, P.; Zhu, X.; Wang, J.; Yan, F. Au/Ag core–shell nanocuboids for high-efficiency organic solar cells with broadband plasmonic enhancement. *Energy Environ. Sci.* **2016**, *9*, 898–905. [CrossRef]
23. Mahajan, P.; Singh, A.; Datt, R.; Gupta, V.; Arya, S. Realization of inverted organic solar cells by using sol-gel synthesized ZnO/Y_2O_3 core/shell nanoparticles as electron transport layer. *IEEE J. Photovolt.* **2020**, *10*, 1744–1749. [CrossRef]
24. Ng, A.; Yiu, W.K.; Foo, Y.; Shen, Q.; Bejaoui, A.; Zhao, Y.; Gokkaya, H.C.; Djuris, A.B.; Zapien, J.A.; Chan, W.K.; et al. Enhanced performance of PTB7: PC71BM solar cells via different morphologies of gold nanoparticles. *ACS Appl. Mater. Interfaces* **2014**, *6*, 20676–20684. [CrossRef]
25. Gollu, S.R.; Sharma, R.; Srinivas, G.; Kundu, S.; Gupta, D. Effects of incorporation of copper sulfide nanocrystals on the performance of P3HT: PCBM based inverted solar cells. *Org. Electron.* **2014**, *15*, 2518–2525. [CrossRef]
26. Cardozo, O.; Farooq, S.; Farias, P.M.; Fraidenraich, N.; Stingl, A.; Araujo, R.E.D. Zinc oxide nanodiffusers to enhance p3ht: Pcbm organic solar cells performance. *J. Mater. Sci. Mater. Electron.* **2022**, *33*, 3225–3236. [CrossRef]
27. Sundaram, P.S.; Sangeetha, T.; Rajakarthihan, S.; Vijayalaksmi, R.; Elangovan, A.; Arivazhagan, G. XRD structural studies on cobalt doped zinc oxide nanoparticles synthesized by coprecipitation method: Williamson-Hall and size-strain plot approaches. *Phys. B Condens. Matter* **2020**, *595*, 412342. [CrossRef]
28. Synthesis, S.I. Synthesis, properties and applications of semiconductor nanostructured zinc sulfide. *Russ. Chem. Rev.* **2019**, *88*, 571. [CrossRef]
29. Hoy-Benítez, J.A.; Colina-Ruiz, R.A.; Lezama-Pacheco, J.S.; de León, J.M.; Espinosa-Faller, F.J. Local atomic structure and lattice defect analysis in heavily Co-doped ZnS thin films using X-ray absorption fine structure spectroscopy. *J. Phys. Chem. Solids* **2020**, *136*, 109154. [CrossRef]

30. Ullah, A.; Javaid, N.; Rafiq, A.; Samreen, A.; Riaz, S.; Naseem, S. Outstanding performance of Co-doped ZnS nanoparticles used as nanocatalyst for synthetic dye degradation. *Results Mater.* **2024**, *24*, 100628. [CrossRef]
31. Salem, J.K.; Hammad, T.M.; Kuhn, S.; Draaz, M.A.; Hejazy, N.K.; Hempelmann, R. Structural and optical properties of Co-doped ZnS nanoparticles synthesized by a capping agent. *J. Mater. Sci. Mater. Electron.* **2014**, *25*, 2177–2182. [CrossRef]
32. Iranmanesh, P.; Saeednia, S.; Nourzpoor, M. Characterization of ZnS nanoparticles synthesized by co-precipitation method. *Chin. Phys. B* **2015**, *24*, 046104. [CrossRef]
33. Mohamed, W.S.; Ezzeldien, M.; Alshammari, A.H.; Alshammari, K.; Alhassan, S.; Hadia, N.M.A. Facile hydrothermal synthesis and characterization of novel Co-doped ZnS nanoparticles with superior physical properties. *Opt. Mater.* **2024**, *157*, 116345. [CrossRef]
34. Wang, C.; MacKenzie, R.C.; Würfel, U.; Neher, D.; Kirchartz, T.; Deibel, C.; Saladina, M. Transport resistance dominates the fill factor losses in record organic solar cells. *Adv. Energy Mater.* **2025**, 2405889. [CrossRef]
35. Mousavifar, S.M.; Ghasemi, M.; Haidari, G. Near and far-field plasmonic enhancement from thermally evaporated ag nanostructures in polymer photovoltaic cells: Simulation and experimental study. *IEEE J. Photovolt.* **2020**, *10*, 1735–1743. [CrossRef]
36. Zhang, X.G.; Pantelides, S.T. Theory of space charge limited currents. *Phys. Rev. Lett.* **2012**, *108*, 266602. [CrossRef]
37. Yang, M.; Fu, S.; Wang, L.; Ren, M.; Li, H.; Han, S.; Lu, X.; Lu, F.; Tong, J.; Li, J. Efficient organic solar cells by modulating photoactive layer morphology with halogen-free additives. *Opt. Mater.* **2023**, *137*, 113503. [CrossRef]
38. Waketola, A.G.; Hone, F.G.; Geldasa, F.T.; Genene, Z.; Mammo, W.; Tegegne, N.A. Enhancing the performance of wide-bandgap polymer-based organic solar cells through silver nanorod integration. *ACS Omega* **2024**, *9*, 8082–8091. [CrossRef]

Disclaimer/Publisher's Note: The statements, opinions and data contained in all publications are solely those of the individual author(s) and contributor(s) and not of MDPI and/or the editor(s). MDPI and/or the editor(s) disclaim responsibility for any injury to people or property resulting from any ideas, methods, instructions or products referred to in the content.